Pergamon

Int. J. Solids Structures Vol. 31, No. 14, pp. 1949–1965, 1994
Elsevier Science Ltd
Printed in Great Britain
0020-7683/94 $7.00 + .00

0020-7683(94)E0018-Q

FAILURE ANALYSIS OF AIRCRAFT ENGINE DISKS II

GUIDO DHONDT
MTU Motoren- und Turbinen-Union München GmbH, Postfach 500640, 80976 München, Germany

(*Received* 9 *August* 1993; *in revised form* 25 *October* 1993)

Abstract—Aircraft engine disks frequently show multiple failures when collapsing due to a radial crack. This subject has been treated previously by a simplified theory including bending effects only. In this article a more elaborate analysis has been performed, including extensional, torsional, shear and rotational inertia effects. It is shown that, contrary to the simplified theory, the wave speed remains finite for high wave numbers. An explicit finite difference scheme of the governing differential equations is derived and the conditions for its stability are examined. Application to the stress analysis of a rotating disk immediately after radial failure reveals that a propagating and gradually increasing axial stress maximum emanates from the crack which will generally lead to additional failures at about 100–140° away from the first failure.

1. INTRODUCTION

Aircraft engine disk testing in spin pit facilities has shown that the disks frequently break up in more than two parts when failing. In a lot of cases three equally sized parts were recovered. This phenomenon has already been treated recently by means of a simplified theory (Köhl and Dhondt, 1993). It was shown that after a radial failure, the bending moment increases rapidly and exhibits a maximum which moves away from the crack while increasing continuously. This frequently leads to additional failures about 120° away from the first failure. However, a drawback of the simplified theory is the prediction of an infinite wave speed for large wave numbers which causes the whole disk to respond instantaneously to a locally confined disturbance.

The theory in the present article uses all six degrees of freedom in each point of the axis of the disk (three displacements and three rotations), and was first introduced by Bickford and Strom (1975). It leads to six coupled partial differential equations to be complemented by the appropriate initial and boundary conditions and includes extensional, torsional, shear and rotational inertia effects. It yields a finite wave speed even for large wave numbers.

In the following sections the governing equations are given and an explicit finite difference scheme is introduced. Satisfaction of the Neumann stability yields a maximum size of the time step. Application of the method to the problem of a sudden radial failure in an aircraft engine disk shows that, soon after the failure, the in-plane bending moments and axial stresses exhibit a maximum along the disk which increases and propagates away from the crack. The present theory agrees with the earlier simple theory in that this phenomenon will frequently lead to a second failure about 100–140° away from the first failure. However, due to the finite wave speed the propagating maximum is more outspoken, though not increasing so fast.

2. GOVERNING EQUATIONS

The basic theory has been developed by Bickford and Strom (1975). The aircraft engine disk is modelled as a curved beam with constant curvature k (Fig. 1). The motion of a point of the beam is expressed as a Taylor series about the centerline. Only linear terms are kept. Furthermore, it is assumed that the in-plane strains are negligible;

$$e_{xx} = e_{yy} = e_{xy} = 0. \tag{1}$$

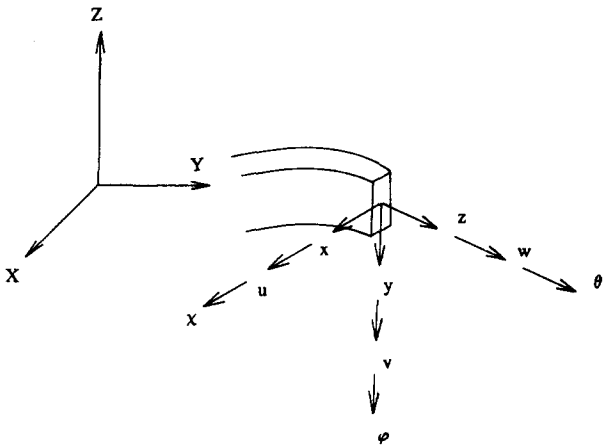

Fig. 1. Curved beam segment with local axes and displacements.

This leads to

$$\begin{aligned} U(x,y,z,t) &= u(z,t)-y\theta(z,t) \\ V(x,y,z,t) &= v(z,t)+x\theta(z,t) \\ W(x,y,z,t) &= w(z,t)-x\varphi(z,t)+y\chi(z,t) \end{aligned} \tag{2}$$

where U, V and W are the displacements of an arbitrary point of the beam, whereas u, v, w and χ, φ, θ represent the displacements and rotations of a point on the axis, respectively. The nonzero strains can be expressed as

$$\begin{aligned} ge_{zz} &= w'-ku-x\varphi'+y(\chi'+k\theta) \\ 2ge_{xz} &= u'+kw-\varphi-y(\theta'-k\chi) \\ 2ge_{yz} &= v'+\chi+x(\theta'-k\chi) \end{aligned} \tag{3}$$

where $g = 1-kx$, and $' = \partial/\partial z$. The force resultants are introduced by (the Poisson effect in the normal stress–strain relationship has been discarded)

$$\begin{aligned} N &= \int\int \sigma_{zz}\,\mathrm{d}A = \int\int Ee_{zz}\,\mathrm{d}A \\ V_x &= \int\int \sigma_{xz}\,\mathrm{d}A = \int\int 2Ge_{xz}\,\mathrm{d}A \\ V_y &= \int\int \sigma_{yz}\,\mathrm{d}A = \int\int 2Ge_{yz}\,\mathrm{d}A \\ M_x &= \int\int y\sigma_{zz}\,\mathrm{d}A = \int\int Eye_{zz}\,\mathrm{d}A \\ M_y &= -\int\int x\sigma_{zz}\,\mathrm{d}A = -\int\int Exe_{zz}\,\mathrm{d}A \\ T &= \int\int (x\sigma_{yz}-y\sigma_{xz})\,\mathrm{d}A = \int\int 2G(xe_{yz}-ye_{xz})\,\mathrm{d}A \end{aligned} \tag{4}$$

where E is Young's modulus, G is the shear modulus and A the cross sectional area.

Substitution of eqn (3) into eqn (4) yields

$$\begin{aligned}
N &= EI_{00}(w'-ku)-E\varphi' I_{10}+E(\chi'+k\theta)I_{01}\\
V_x &= G(u'+kw-\varphi)I_{00}-G(\theta'-k\chi)I_{01}\\
V_y &= G(v'+\chi)I_{00}+G(\theta'-k\chi)I_{10}\\
M_x &= EI_{01}(w'-ku)-E\varphi' I_{11}+E(\chi'+k\theta)I_{02}\\
M_y &= -E(w'-ku)I_{10}+E\varphi' I_{20}-E(\chi'+k\theta)I_{11}\\
T &= G(v'+\chi)I_{10}+G(\theta'-k\chi)(I_{20}+I_{02})-G(u'+kw-\varphi)I_{01}
\end{aligned} \tag{5}$$

where

$$I_{ij} = \int\int \frac{x^i y^j \,\mathrm{d}A}{1-kx}. \tag{6}$$

Application of Hamilton's Principle to the rotating disk leads to six coupled partial differential equations:

$$\begin{aligned}
&G(u''+kw'-\varphi')I_{00}-G(\theta''-k\chi')I_{01}+kEI_{00}(w'-ku)-kE\varphi' I_{10}+kE(\chi'+k\theta)I_{01}\\
&\qquad -A\rho\ddot{u}-\rho kJ_{11}\ddot{\theta} = p;\\
&G(v''+\chi')I_{00}+G(\theta''-k\chi')I_{10}-A\rho\ddot{v}+\rho kJ_{20}\ddot{\theta} = 0;\\
&EI_{00}(w''-ku')-E\varphi'' I_{10}+E(\chi''+k\theta')I_{01}-kG(u'+kw-\varphi)I_{00}+kG(\theta'-k\chi)I_{01}\\
&\qquad -A\rho\ddot{w}+\rho kJ_{11}\ddot{\chi}-\rho kJ_{20}\ddot{\varphi} = 0;\\
&E(w''-ku')I_{01}-E\varphi'' I_{11}+E(\chi''+k\theta')I_{02}+kG(v'+\chi)I_{10}\\
&\quad +kG(\theta'-k\chi)(I_{20}+I_{02})-kG(u'+kw-\varphi)I_{01}-G(v'+\chi)I_{00}-G(\theta'-k\chi)I_{10}\\
&\qquad -\rho(J_{02}-kJ_{12})\ddot{\chi}+\rho(J_{11}-kJ_{21})\ddot{\varphi}+\rho kJ_{11}\ddot{w} = 0;\\
&-E(w''-ku')I_{10}+E\varphi'' I_{20}-E(\chi''+k\theta')I_{11}+G(u'+kw-\varphi)I_{00}-G(\theta'-k\chi)I_{01}\\
&\qquad -\rho(J_{20}-kJ_{30})\ddot{\varphi}+\rho(J_{11}-kJ_{21})\ddot{\chi}-\rho kJ_{20}\ddot{w} = 0;\\
&G(v''+\chi')I_{10}+G(\theta''-k\chi')(I_{20}+I_{02})-G(u''+kw'-\varphi')I_{01}-kE(w'-ku)I_{01}\\
&\quad +kE\varphi' I_{11}-kE(\chi'+k\theta)I_{02}-\rho(J-k(J_{12}+J_{30}))\ddot{\theta}-\rho kJ_{11}\ddot{u}+\rho kJ_{20}\ddot{v} = 0
\end{aligned} \tag{7}$$

where

$$J_{ij} = \int\int x^i y^j \,\mathrm{d}A, \tag{8}$$

$\cdot = \partial/\partial t$, $J = J_{02}+J_{20}$ and ρ is the mass density. p represents the centrifugal loading

$$p = 2\pi\rho V f^2 \tag{9}$$

where f is the frequency (Hz) and V the total volume of the disk.

In the governing eqns (7), the effects of shear deformation, rotational inertia and extensionality are included. They have to be complemented by the appropriate boundary and initial conditions.

The problem of the failing disk is symmetric about the failure (Fig. 2). Immediately after cracking, the boundary conditions can be expressed as

$$\begin{aligned}
N = V_x = V_y = M_x = M_y = T = 0 \quad &\text{at } z = 0\\
u' = v' = w = \chi = \varphi = \theta' = 0 \quad &\text{at } z = L
\end{aligned} \tag{10}$$

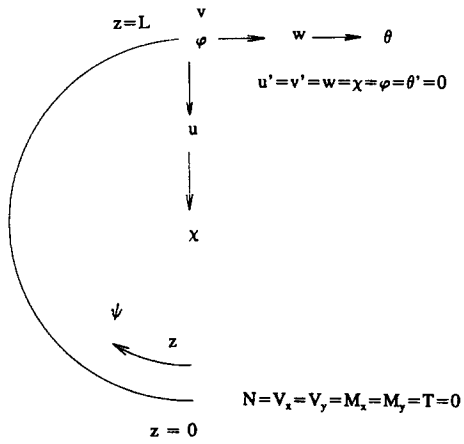

Fig. 2. Boundary conditions at $z = 0$ and $z = L$.

where L is half the circumference of the disk. The initial conditions (immediately before cracking) amount to

$$\begin{aligned} &u = u_0 \\ &\theta = \theta_0 \\ &v = w = \chi = \varphi = 0 \\ &\dot{u} = \dot{v} = \dot{w} = \dot{\chi} = \dot{\varphi} = \dot{\theta} = 0 \quad \text{at } t = 0 \end{aligned} \tag{11}$$

where

$$\begin{aligned} u_0 &= \frac{p}{k^2 E}\left(\frac{I_{02}}{I_{01}^2 - I_{00}I_{02}}\right) \\ \theta_0 &= \frac{p}{k^2 E}\left(\frac{I_{01}}{I_{01}^2 - I_{00}I_{02}}\right) \end{aligned} \tag{12}$$

are the radial displacement and torsion angle before failure.

3. DISCRETISATION OF THE GOVERNING EQUATIONS

Equations (7) can be written in the form

$$[\mathbf{H}_1]\ddot{\mathbf{Y}} + [\mathbf{H}_3]\mathbf{Y}'' + [\mathbf{H}_2]\mathbf{Y}' + [\mathbf{H}_4]\mathbf{Y} = \mathbf{P} \tag{13}$$

where

$$\mathbf{Y} = \begin{bmatrix} u \\ v \\ w \\ \chi \\ \varphi \\ \theta \end{bmatrix} \quad \mathbf{P} = \begin{bmatrix} p \\ 0 \\ 0 \\ 0 \\ 0 \\ 0 \end{bmatrix}, \tag{14}$$

$$[\mathbf{H}_1] = \begin{bmatrix} -A\rho & 0 & 0 & 0 & 0 & -\rho k J_{11} \\ \mathrm{s} & -A\rho & 0 & 0 & 0 & \rho k J_{20} \\ \mathrm{s} & \mathrm{s} & -A\rho & \rho k J_{11} & -\rho k J_{20} & 0 \\ \mathrm{s} & \mathrm{s} & \mathrm{s} & -\rho(J_{02}-kJ_{12}) & \rho(J_{11}-kJ_{21}) & 0 \\ \mathrm{s} & \mathrm{s} & \mathrm{s} & \mathrm{s} & -\rho(J_{20}-kJ_{30}) & 0 \\ \mathrm{s} & \mathrm{s} & \mathrm{s} & \mathrm{s} & \mathrm{s} & -\rho(J-k(J_{12}+J_{30})) \end{bmatrix}, \tag{15}$$

$$[\mathbf{H}_2] = \begin{bmatrix} 0 & 0 & k(G+E)I_{00} & k(G+E)I_{01} & -(GI_{00}+kEI_{10}) & 0 \\ \mathrm{a} & 0 & 0 & -G(kI_{10}-I_{00}) & 0 & 0 \\ \mathrm{a} & \mathrm{a} & 0 & 0 & 0 & k(G+E)I_{01} \\ \mathrm{a} & \mathrm{a} & \mathrm{a} & 0 & 0 & kEI_{02}+kG(I_{20}+I_{02})-GI_{10} \\ \mathrm{a} & \mathrm{a} & \mathrm{a} & \mathrm{a} & 0 & -(kEI_{11}+GI_{01}) \\ \mathrm{a} & \mathrm{a} & \mathrm{a} & \mathrm{a} & \mathrm{a} & 0 \end{bmatrix}, \tag{16}$$

$$[\mathbf{H}_3] = \begin{bmatrix} GI_{00} & 0 & 0 & 0 & 0 & -GI_{01} \\ \mathrm{s} & GI_{00} & 0 & 0 & 0 & GI_{10} \\ \mathrm{s} & \mathrm{s} & EI_{00} & EI_{01} & -EI_{10} & 0 \\ \mathrm{s} & \mathrm{s} & \mathrm{s} & EI_{02} & -EI_{11} & 0 \\ \mathrm{s} & \mathrm{s} & \mathrm{s} & \mathrm{s} & EI_{20} & 0 \\ \mathrm{s} & \mathrm{s} & \mathrm{s} & \mathrm{s} & \mathrm{s} & G(I_{20}+I_{02}) \end{bmatrix}, \tag{17}$$

$$[\mathbf{H}_4] = \begin{bmatrix} -k^2EI_{00} & 0 & 0 & 0 & 0 & k^2EI_{01} \\ \mathrm{s} & 0 & 0 & 0 & 0 & 0 \\ \mathrm{s} & \mathrm{s} & -k^2GI_{00} & -k^2GI_{01} & kGI_{00} & 0 \\ \mathrm{s} & \mathrm{s} & \mathrm{s} & G(2kI_{10}-I_{00}-k^2(I_{20}+I_{02})) & kGI_{01} & 0 \\ \mathrm{s} & \mathrm{s} & \mathrm{s} & \mathrm{s} & -GI_{00} & 0 \\ \mathrm{s} & \mathrm{s} & \mathrm{s} & \mathrm{s} & \mathrm{s} & -k^2EI_{02} \end{bmatrix}. \tag{18}$$

$[\mathbf{H}_1]$, $[\mathbf{H}_3]$ and $[\mathbf{H}_4]$ are symmetric (symbol s), $[\mathbf{H}_2]$ is antisymmetric (symbol a). Discretisation of the partial derivatives in eqn (13)

$$\ddot{\mathbf{Y}} = \frac{1}{h^2}(\mathbf{Y}_{r+1,s}-2\mathbf{Y}_{r,s}+\mathbf{Y}_{r-1,s})$$

$$\mathbf{Y}' = \frac{1}{2l}(\mathbf{Y}_{r,s+1}-\mathbf{Y}_{r,s-1})$$

$$\mathbf{Y}'' = \frac{1}{l^2}(\mathbf{Y}_{r,s+1}-2\mathbf{Y}_{r,s}+\mathbf{Y}_{r,s-1}), \tag{19}$$

where h and l are the step sizes in t and z, respectively and $\mathbf{Y}_{r,s}$ denotes the value of $\mathbf{Y}$ at the discretisation point (r, s) (r changes with t and s with z), leads to the following explicit scheme:

$$[\alpha]\mathbf{Y}_{r+1,s} = \mathbf{P}-[\beta]\mathbf{Y}_{r,s-1}-[\gamma]\mathbf{Y}_{r,s}-[\delta]\mathbf{Y}_{r,s+1}-[\varepsilon]\mathbf{Y}_{r-1,s} \tag{20}$$

where

$$[\alpha] = \frac{[\mathbf{H}_1]}{h^2}$$
$$[\beta] = \frac{[\mathbf{H}_3]}{l^2} - \frac{[\mathbf{H}_2]}{2l}$$
$$[\gamma] = -2\frac{[\mathbf{H}_1]}{h^2} - 2\frac{[\mathbf{H}_3]}{l^2} + [\mathbf{H}_4]$$
$$[\delta] = \frac{[\mathbf{H}_3]}{l^2} + \frac{[\mathbf{H}_2]}{2l}$$
$$[\varepsilon] = [\alpha]. \tag{21}$$

The boundary conditions [eqn (10)] at $z = 0$ (corresponds to $s = 0$) together with eqn (5) can be written as

$$[\mathbf{A}]\mathbf{Y}_{r,-1} + [\mathbf{B}]\mathbf{Y}_{r,0} + [\mathbf{C}]\mathbf{Y}_{r,1} = 0 \tag{22}$$

where

$$[\mathbf{A}] = \frac{1}{2l}\begin{bmatrix} -GI_{00} & 0 & 0 & 0 & 0 & GI_{01} \\ 0 & -GI_{00} & 0 & 0 & 0 & -GI_{10} \\ 0 & 0 & -EI_{00} & -EI_{01} & EI_{10} & 0 \\ 0 & 0 & -EI_{01} & -EI_{02} & EI_{11} & 0 \\ 0 & 0 & EI_{10} & EI_{11} & -EI_{20} & 0 \\ GI_{01} & -GI_{10} & 0 & 0 & 0 & -G(I_{02}+I_{20}) \end{bmatrix} \tag{23}$$

$$[\mathbf{B}] = \begin{bmatrix} 0 & 0 & kGI_{00} & kGI_{01} & -GI_{00} & 0 \\ 0 & 0 & 0 & G(I_{00}-kI_{10}) & 0 & 0 \\ -kEI_{00} & 0 & 0 & 0 & 0 & kEI_{01} \\ -kEI_{01} & 0 & 0 & 0 & 0 & kEI_{02} \\ kEI_{10} & 0 & 0 & 0 & 0 & -kEI_{11} \\ 0 & 0 & -kGI_{01} & G[I_{10}-k(I_{02}+I_{20})] & GI_{01} & 0 \end{bmatrix} \tag{24}$$

$$[\mathbf{C}] = -[\mathbf{A}]. \tag{25}$$

Once $\mathbf{Y}_{r,s}$, $-1 \leqslant s \leqslant n+1$ are known, eqn (20) allows for the solution of $\mathbf{Y}_{r+1,s}$, $0 \leqslant s \leqslant n$. The boundary conditions at $z = 0$ [eqn (22)] yield $\mathbf{Y}_{r+1,-1}$. The boundary conditions at $z = L$ (corresponds to $s = n$) [eqn (10)] consist of Dirichlet conditions for w, χ and φ and Neumann conditions for u, v and θ. The Dirichlet condition e.g. for w, leads to an explicit substitution of $w_{r+1,n}$ and, by expressing the first spatial derivative at $z = L$ with two different schemes (both of second order accuracy)

$$\frac{3w_{r+1,n} + w_{r+1,n-2} - 4w_{r+1,n-1}}{2l} = \frac{w_{r+1,n+1} - w_{r+1,n-1}}{2l}, \tag{26}$$

to $w_{r+1,n+1}$. The Neumann conditions, e.g. for u, lead to

$$u_{r+1,n+1} = u_{r+1,n-1}. \tag{27}$$

In this way all values of $\mathbf{Y}_{r+1,s}$, $-1 \leqslant s \leqslant n+1$ are determined.

The Dirichlet initial conditions are easily satisfied. The Neumann initial conditions are satisfied by taking the same values for two consecutive time steps at the start.

4. NUMERICAL STABILITY

The numerical stability of the explicit scheme is checked by applying the Neumann stability test (Lapidus and Pinder, 1982). To this end a solution of the form

$$\mathbf{Y}_{r,s} = \xi^r \, e^{ilsμ} \, X \tag{28}$$

is substituted into the homogeneous form of eqn (20). Solutions of ξ as a function of the arbitrary parameter μ are looked for. The Neumann stability requires the nonexistence of growing homogeneous solutions, i.e.

$$|\xi| \leqslant 1 \tag{29}$$

for all μ must be satisfied. A non-trivial solution is obtained for

$$|\xi^2[\alpha]+\xi([\beta]\, e^{-i\mu l}+[\gamma]+[\delta]\, e^{i\mu l})+[\varepsilon]| = 0. \tag{30}$$

Substitution of eqn (21) into eqn (30) leads to

$$\left| -\left\{\frac{[\mathbf{H}_3]}{l^2}(\cos \mu l - 1) - \frac{[\mathbf{H}_1]}{h^2} + \frac{[\mathbf{H}_4]}{2} + i\frac{[\mathbf{H}_2]}{2l}\sin \mu l\right\} - \lambda\left\{\frac{-[\mathbf{H}_1]}{h^2}\right\}\right| = 0 \tag{31}$$

where

$$\lambda = -\frac{\xi^2+1}{2\xi}. \tag{32}$$

Equation (31) is a generalised eigenvalue equation of the form

$$|[\mathbf{G}]-\lambda[\mathbf{H}]| = 0 \tag{33}$$

where [G] is hermitian and [H] is symmetric and positive definite since the total kinetic energy of the beam can be expressed as (Bickford and Strom, 1975)

$$K = -\int_0^L \frac{1}{2}\dot{\mathbf{Y}}^T[\mathbf{H}_1]\dot{\mathbf{Y}}\, dz. \tag{34}$$

Thus the eigenvalues λ of eqn (31) are real (Zurmühl and Falk, 1984). Equation (29) can be satisfied only if

$$|\lambda| \leqslant 1 \tag{35}$$

for all values of μ. Making the substitution $\mu l = \psi$, for a given beam geometry and step sizes h and l, the explicit scheme will be numerically stable if all eigenvalues λ of

$$\left|[\alpha]^{-1}\left\{\frac{[\mathbf{H}_3]}{l^2}(\cos \psi - 1) - \frac{[\mathbf{H}_1]}{h^2} + \frac{[\mathbf{H}_4]}{2} + i\frac{[\mathbf{H}_2]}{2l}\sin \psi\right\} - \lambda[I]\right| = 0 \tag{36}$$

satisfy eqn (35) with $0 \leqslant \psi \leqslant \pi$. This condition is satisfied for a small enough time step h.

5. DISPERSION CURVES

The dispersion curves are obtained by substituting the wave form

$$\mathbf{Y}(z, t) = X\, e^{i(\gamma z - \omega t)} \tag{37}$$

into the homogeneous form of eqn (13). This leads to a non-trivial solution only if

$$|\{-\gamma^2[\mathbf{H}_3]+[\mathbf{H}_4]+[\mathbf{H}_2]i\gamma\}-\omega^2[\mathbf{H}_1]| = 0. \tag{38}$$

This is again an equation of the form in eqn (33) and yields real eigenvalues for $\lambda = \omega^2$. In the remainder of this article the following non-dimensionalised forms of the wavenumber γ, the circular frequency ω and wave velocity c will be used:

$$\bar{\gamma} = K\gamma \tag{39}$$

$$\bar{\omega} = \frac{\omega K}{c_0} \tag{40}$$

$$\bar{c} = \frac{c}{c_0} = \frac{\omega}{\gamma c_0} \tag{41}$$

where

$$K = \sqrt{\frac{J_{20}}{A}} \tag{42}$$

$$c_0 = \sqrt{\frac{E}{\rho}}. \tag{43}$$

6. DISK WITH A RECTANGULAR CROSS SECTION

For a first qualitative understanding a small disk with a simple rectangular cross section (Fig. 3; all dimensions are in mm) is analysed. For the material properties $E = 210\,000$ MPa, $\nu = 0.3$ and $\rho = 8000$ kg/m^3 were taken. The rotational speed was $f = 52180$ revolutions/min. For the present geometry $k = 0.05$ mm^{-1}.

The stability curves for $l = \pi/100k$ and $h = 0.25\ 10^{-7}$ s are depicted in Fig. 4. Since $|\lambda| \leqslant 1$ these step sizes yield a stable explicit scheme. For larger h-values the curves move downwards into the negative λ-range to yield an unstable scheme for $\lambda < -1$.

The dispersion curves in Fig. 5 agree very well with the ones found by Graff (1970). For large wave numbers the wave velocity remains finite. This is not the case for the simplified theory published earlier (Köhl and Dhondt, 1993) for which the dispersion curves are represented in Fig. 6. The improvement of the present theory is largely due to the inclusion of the rotational inertia and shear deformation and is comparable with the

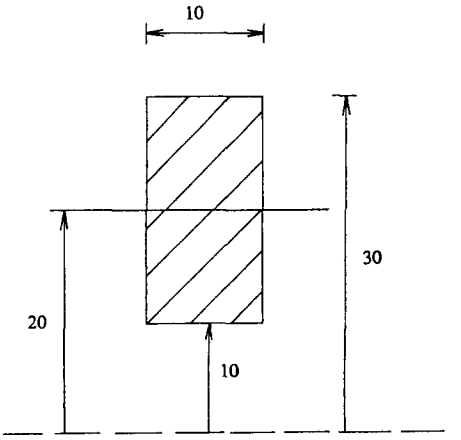

Fig. 3. Disk with rectangular cross section.

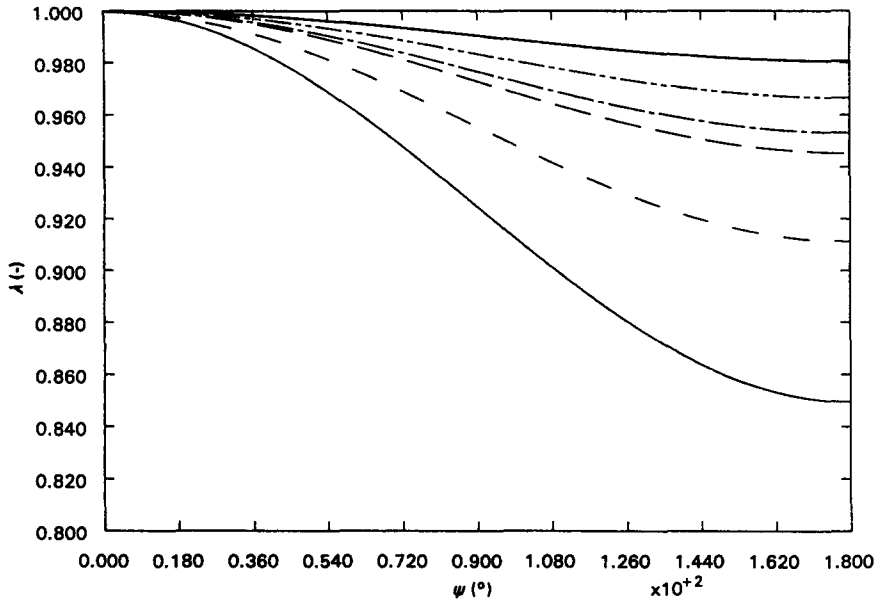

Fig. 4. Stability curves for $h = 0.25 \times 10^{-7}$ s.

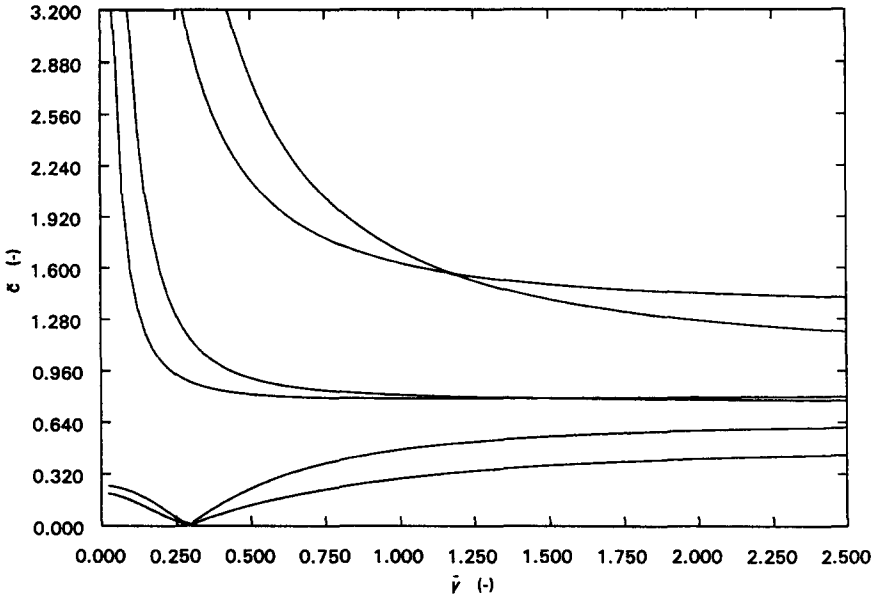

Fig. 5. Dispersion curves for the rectangular beam.

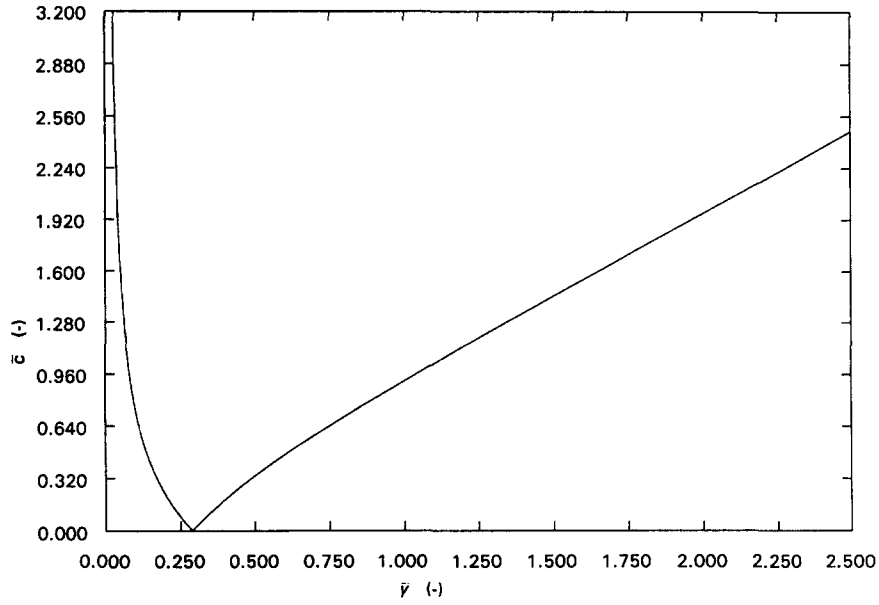

Fig. 6. Dispersion curves for the simplified theory.

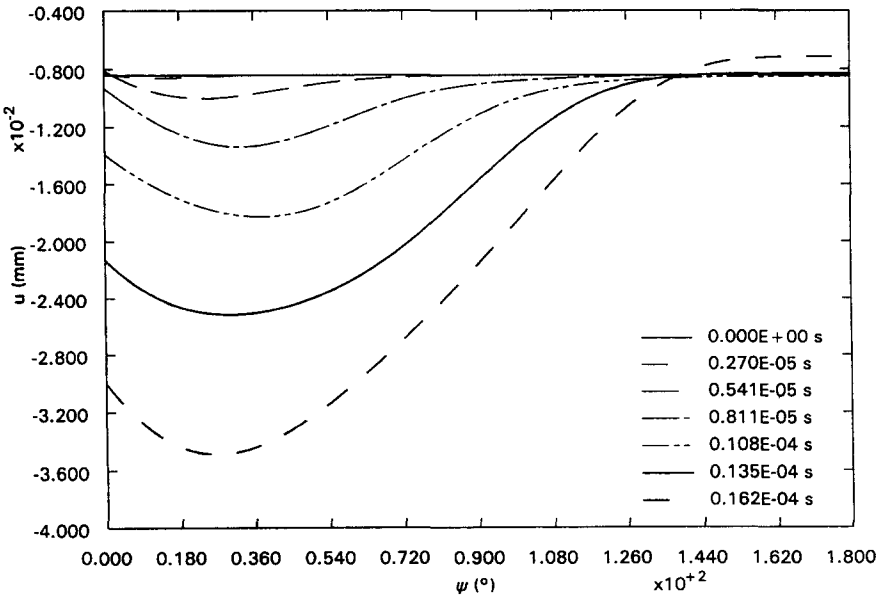

Fig. 7. Tangential in-plane displacement u.

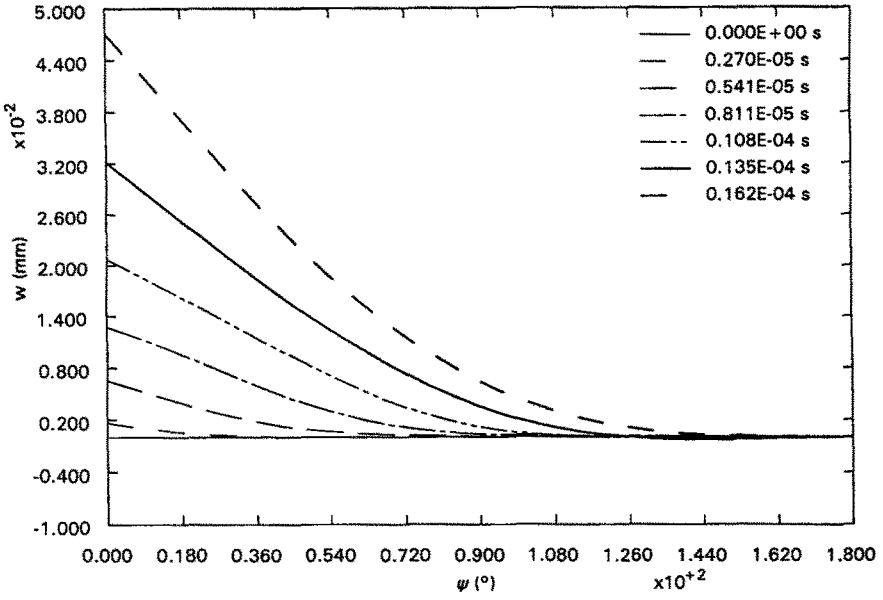

Fig. 8. Axial in-plane displacement w.

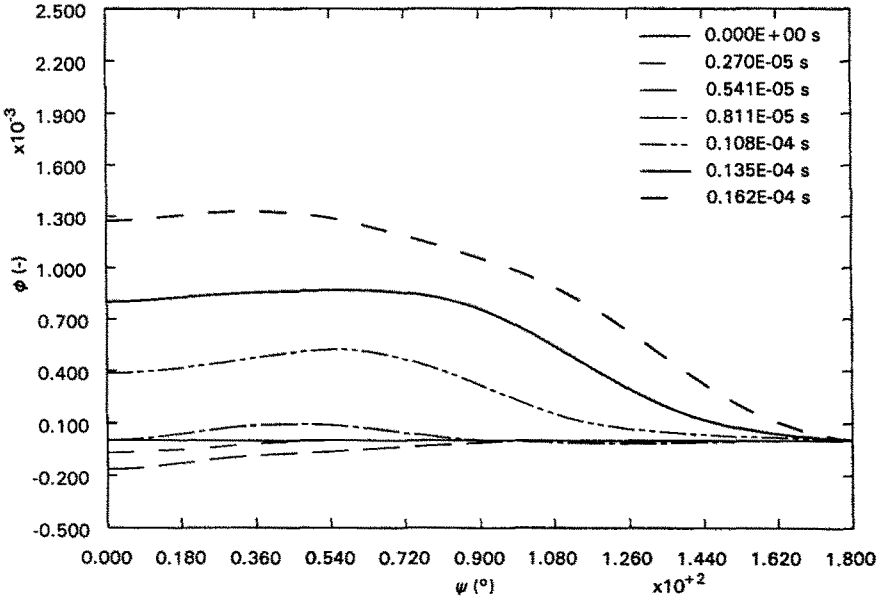

Fig. 9. In-plane bending angle φ.

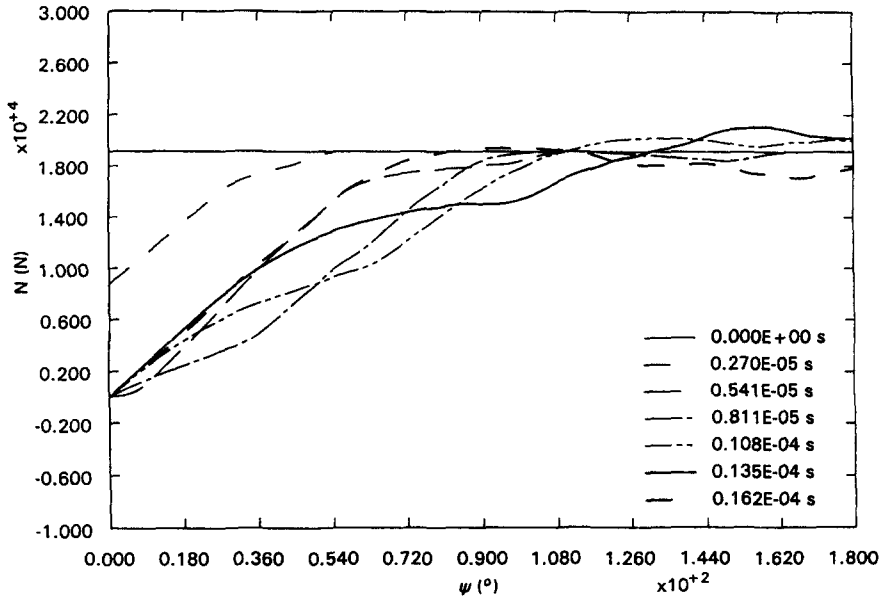

Fig. 10. Axial force N.

difference between the Bernoulli–Euler and Timoshenko beam theories for the straight beam (Graff, 1975).

Figures 7–12 show the displacements and internal forces immediately after fracture as a function of the angle $\psi = kz$ (Fig. 2). Fracture itself was not introduced suddenly but was spread out over about 200 time steps. The finite wave speed allows for a gradual propagation of the fracture signal. It results in a slower growth of the internal forces as can be seen by comparing Fig. 12 with Fig. 13, the latter of which represents the in-plane

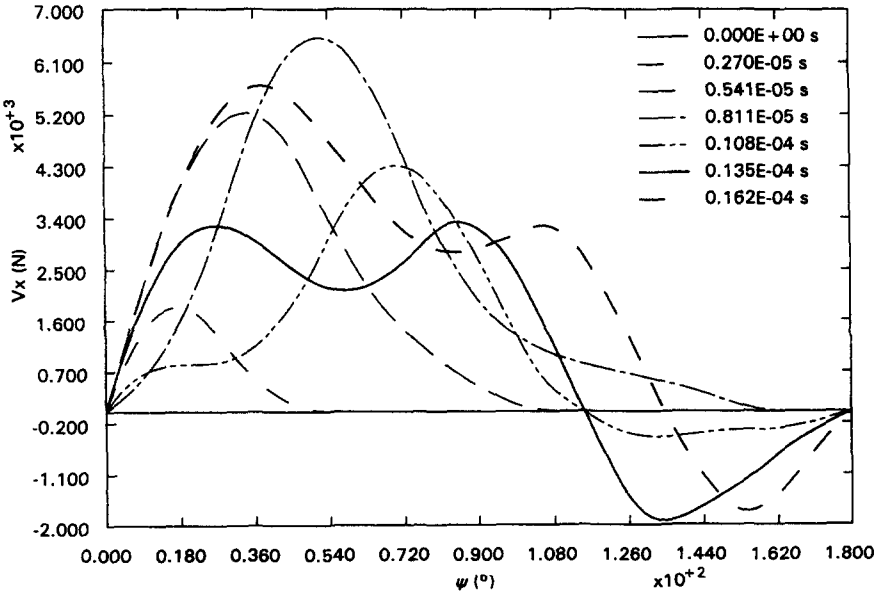

Fig. 11. In-plane shear force V_x.

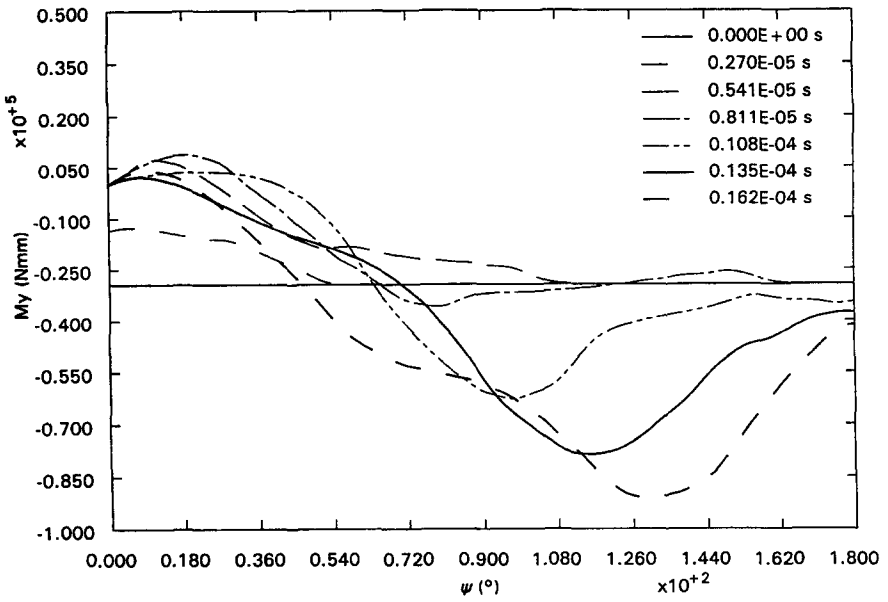

Fig. 12. In-plane bending moment M_y.

bending moment obtained by the simplified theory. However, just like in the simplified theory, the bending moment has a maximum over the disk range, which propagates gradually towards $z = L$. The same observation applied to the axial stresses at the inside of the beam (Fig. 14). The growing axial stress exceeds its pre-fracture value at about 60° away from the fracture location and increases steadily while propagating towards the symmetry plane.

Table 1 gives the location and the value of the stress maximum at different times.

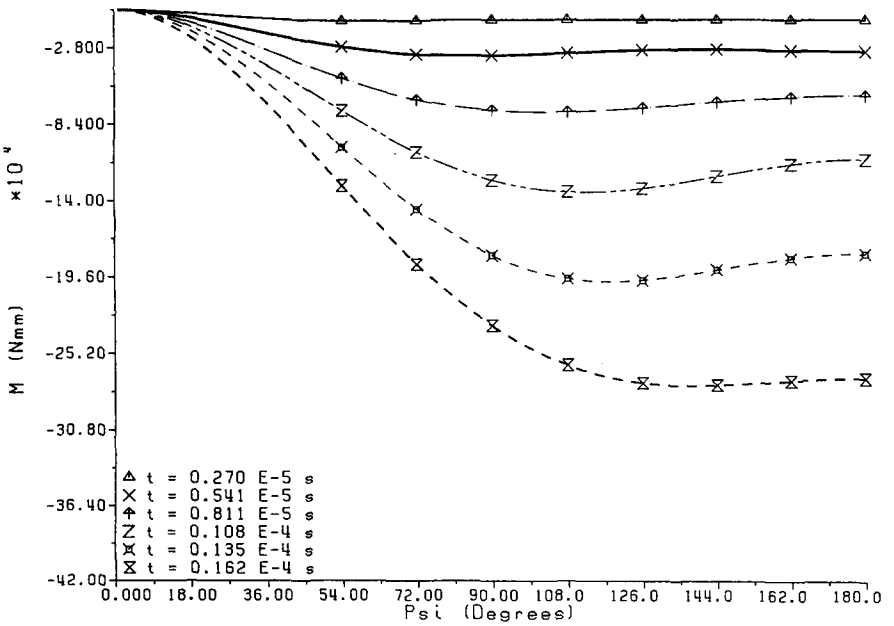

Fig. 13. In-plane bending moment in the simplified theory.

Table 1. Location and value of the axial stress maximum

Time (s)	Maximum stress location ψ (°)	Maximum stress/ pre-fracture stress
0.811×10^{-5}	80–100	1.02
0.108×10^{-4}	100	1.47
0.135×10^{-4}	115	1.74
0.162×10^{-4}	130	1.94

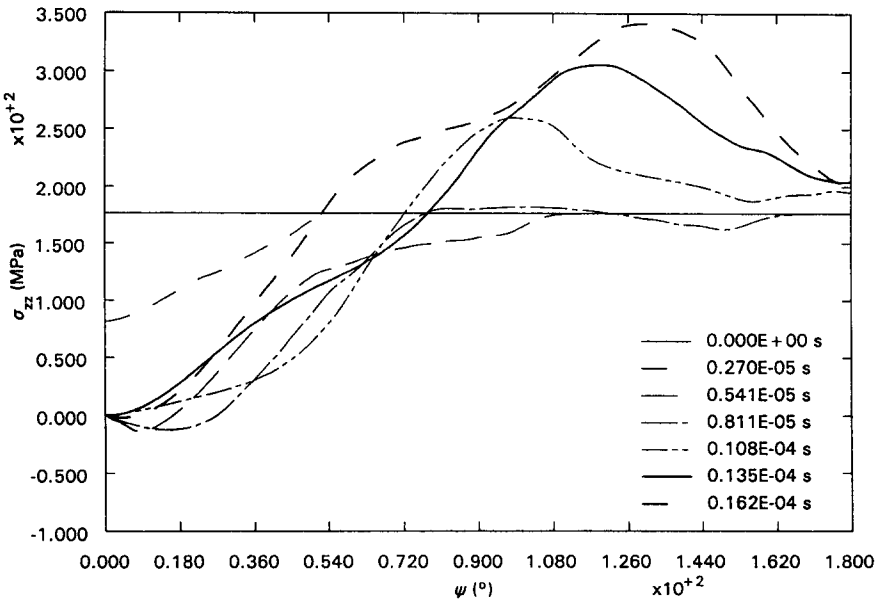

Fig. 14. Axial stress σ_{zz}.

Assuming a disk design such that the pre-fracture stress amounts to the proportional limit of the material and taking the value of the ultimate tensile strength divided by the proportional limit to be in the range 1.2–2.0, it is clear that an additional fracture will occur at about 90°–140°.

7. ENGINE DISK

The same engine disk (Fig. 15) already treated in a previous article (Köhl and Dhondt, 1993) was examined with the present theory. At first a simplified geometry, not taking the asymmetry into account, was introduced ($k = 0.01919$ mm^{-1}) and the axial stress at the inside of the disk immediately after failure was calculated (Fig. 16). It exhibits the same characteristics as in the case of the rectangular disk; at $z = 0$ the stress is reduced to zero. After some time the stress starts to exceed the pre-failure value at about 70° away from the crack. This maximum increases steadily and propagates towards the symmetry plane. Again, for high design stresses, an additional failure about 120° away from the crack is very likely. A more accurate model (Fig. 15) included the asymmetry of the cross section ($k = 0.01989$ mm^{-1}) and led to the torques depicted in Fig. 17. The axial stresses (e.g. in point A, Fig. 18) increased but show the same characteristics as in the simplified geometry model. Depending on the yield strength of the material, plasticity will occur in the bore region.

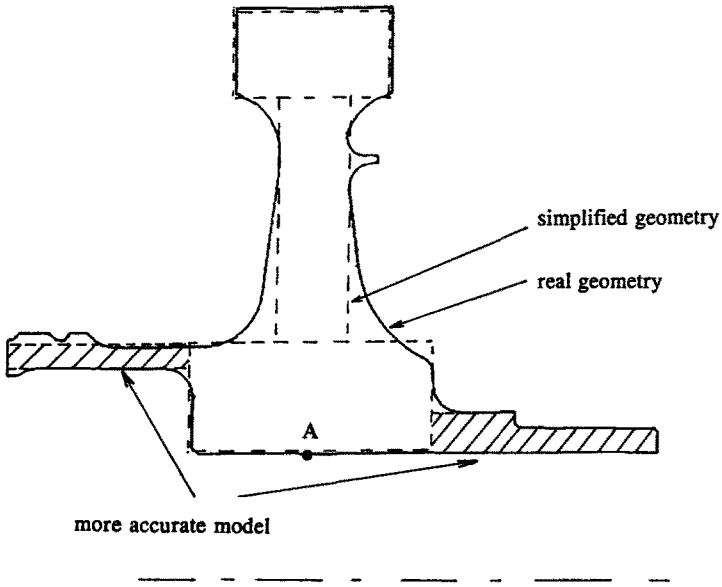

Fig. 15. Engine disk with simplified and more accurate model.

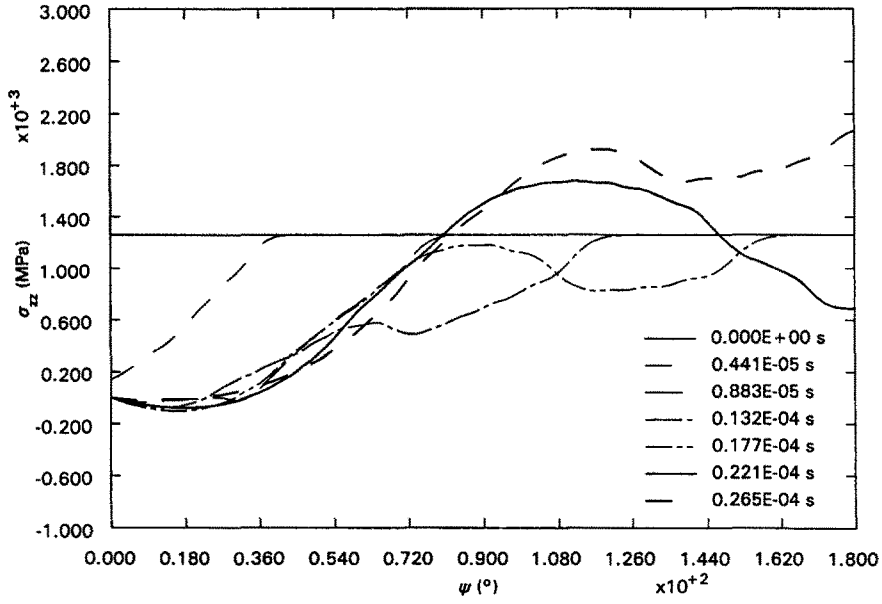

Fig. 16. Axial stresses in the engine disk after fracture (simplified geometry).

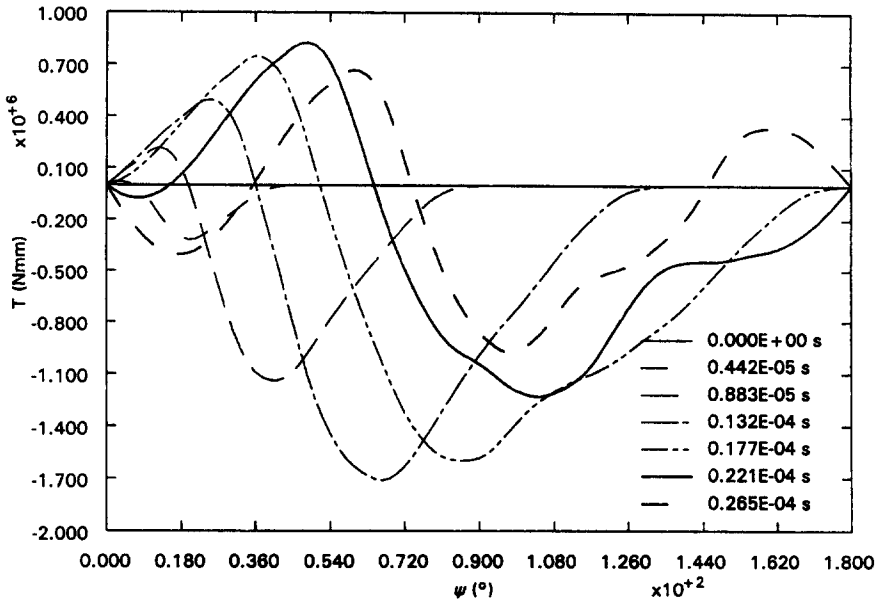

Fig. 17. Torque in the engine disk after fracture.

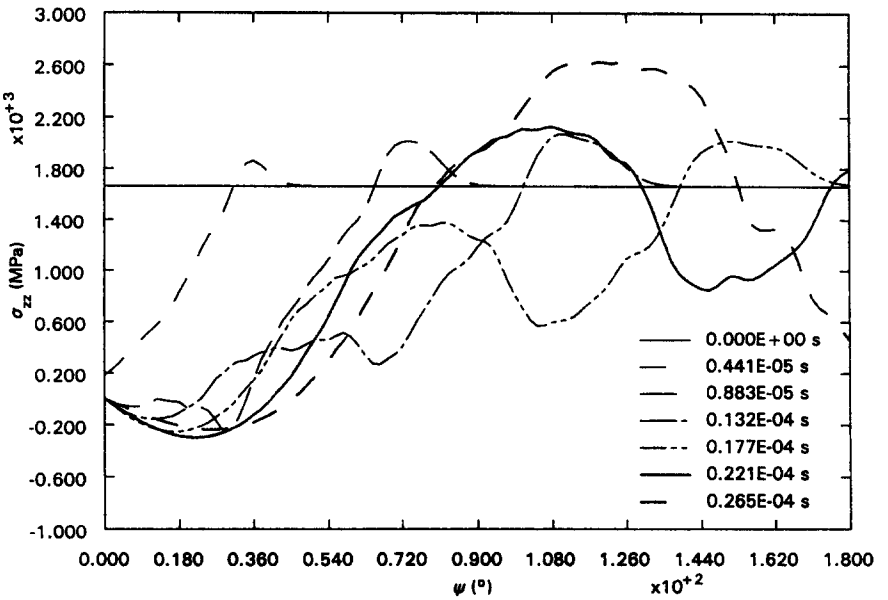

Fig. 18. Axial stresses in the engine disk (point A) after fracture.

8. CONCLUSIONS

A higher order theory including extensional, torsional, shear and rotational inertia effects was used to analyse the problem of a radially failing rotating disk. The governing differential equations were approximated by means of finite differences. It was shown that, after a first failure, a stress maximum propagates along the disk which will frequently lead to a second failure about 100°–140° away from the first failure.

REFERENCES

Bickford, W. B. and Strom, B. T. (1975). Vibration of plane curved beams. *J. Sound Vibr.* **39**(2), 135–146.

Graff, K. F. (1970). Elastic wave propagation in a curved sonic transmission line. *IEEE Trans. Sonics Ultrasonics* **SU17**(1), 1–6.

Graff, K. F. (1975). *Wave Motion in Elastic Solids.* Ohio State University Press.

Köhl, M. and Dhondt, G. (1993). Failure analysis of aircraft engine disks. *Int. J. Solids Structures* **30**(1), 137–149.

Lapidus, L. and Pinder, G. F. (1982). *Numerical Solution of Partial Differential Equations in Science and Engineering.* Wiley, New York.

Zurmühl, R. and Falk, S. (1984). *Matrizen und ihre Anwendungen. Teil 1 : Grundlagen.* Springer-Verlag, Berlin.